Journal of Materials Processing Tech. 321 (2023) 118133

Contents lists available at ScienceDirect

Journal of Materials Processing Tech.

journal homepage: www.elsevier.com/locate/jmatprotec

Fabrication of microlens arrays on single-crystal CaF_2 by ultraprecision diamond turning

Weihai Huang, Kodai Nagayama, Jiwang Yan *

Department of Mechanical Engineering, Faculty of Science and Technology, Keio University, 3–14-1 Hiyoshi, Kohoku-ku, Yokohama 223–8522, Japan

ARTICLE INFO

Associate Editor: Yip-Wah Chung

Keywords:
Single-crystal calcium fluoride
Freeform surface
Diamond turning
Ultraprecision cutting
Soft and brittle materials
Micro lens array

ABSTRACT

Single-crystal calcium fluoride (CaF_2) is considered a superior optical material with good transmittance in a wide transmitted wavelength region. However, the production of high surface quality freeform surfaces on CaF_2 is difficult owing to its soft, brittle, and anisotropic properties. This study attempted to fabricate spherical and hexagonal microlens arrays on CaF_2 using diamond turning with a slow tool servo. In addition, the machining characteristics of CaF_2 were systematically investigated. It was found that microcracks tended to be generated in the cut-in and cut-out regions of the lenses. When cutting along the [− 211] and [11 − 2] directions, the machined surfaces were very prone to cracking. When reducing the maximum undeformed chip thickness to less than approximately 60 nm, continuous ribbon-like chips were formed throughout the cutting process, and all lenses were machined in ductile mode without surface cracking. In addition, a spherical microlens array was successfully fabricated in ductile mode with a surface roughness of approximately 2 nm Sa. Consequently, a hexagonal microlens array with sharp edges and crack-free surfaces was achieved using the proposed depth-offsetting segment cutting method. The surface roughness was approximately 4.1 nm Sa with a form error of approximately 147 nm P-V (peak to valley). Tool wear was insignificant until a machining distance of approximately 50 m; however, with further increase in the machining distance, crater wear and microchipping were observed. This study demonstrated the feasibility of fabricating high-quality freeform microstructured surfaces on CaF_2 and other soft-brittle materials via diamond turning.

1. Introduction

Single-crystal calcium fluoride (CaF_2) is extensively used in optical applications, such as microscopy, photography, and medical laser instruments, owing to its excellent optical performance, including low dispersion, low anomalous dispersion, and good transmittance in a wide transmitted wavelength region (Namba et al., 2004; Huang and Yan, 2023). It exhibits superior optical properties compared to polymers and glass materials in the UV and IR wavelength ranges. Recently, freeform optics have been widely used for virtual reality (VR), augmented reality (AR), displays, and portable/wearable optical devices. Most freeform optics are made of polymers or glass materials using thermal molding processes, such as injection molding (Zhang et al., 2022) or press molding (Zhou et al., 2023). The mold inserts used in molding processes have freeform structures, which are typically fabricated via ultraprecision cutting (Yuan et al., 2020; Zhang et al., 2020a). However, in case of CaF_2 crystals, freeform surfaces cannot be produced by molding processes. The machinability of CaF_2 is poor owing to its low hardness and high brittleness. Consequently, the conventional method for achieving optical surfaces on CaF_2 is grinding, followed by chemical-mechanical polishing (Namba et al., 2005). However, these methods limit the shape flexibility and form accuracy when machining freeform and microstructured surfaces, which are increasingly demanded in advanced optical systems. As an alternative, ultraprecision diamond cutting is an effective method for fabricating freeform surfaces with good surface quality and shape accuracy on brittle materials (Wang et al., 2021; Chen et al., 2022). Several studies attempted to cut freeform surfaces on hard-brittle materials, such as germanium (Li et al., 2017; Guo et al., 2022a) and silicon (Mukaida and Yan, 2017a; Sun et al., 2018). However, CaF_2, which is a soft-brittle material, exhibits a stronger anisotropy of fracture toughness than hard-brittle materials (Huang and Yan, 2023). Moreover, its low hardness and high thermal-expansion coefficient result in unique machining characteristics. Consequently, creating crack-free structured surfaces on CaF_2 is challenging.

Yan et al. (2003) conducted diamond cutting experiments on CaF_2 with straight-nose tools. When machining at large feed rates, the CaF_2

* Corresponding author.
E-mail address: yan@mech.keio.ac.jp (J. Yan).

https://doi.org/10.1016/j.jmatprotec.2023.118133
Received 9 May 2023; Received in revised form 18 July 2023; Accepted 26 August 2023
Available online 28 August 2023

surface generated microcracks similar to other brittle materials such as silicon. However, when machining under wet conditions with extremely low feed rates, instead of forming crack-free surfaces as in silicon, the CaF_2 surface was generated with cracks measuring several hundreds of microns. Such large surface cracks are thought to be caused by the high thermal expansion coefficient of the materials because these cracks disappear when machining is performed under dry conditions. Kakinuma et al. (2015) machined CaF_2 surfaces using diamond turning and characterized their subsurface microstructure. They found that dislocations and subgrains were the primary forms of subsurface damage of CaF_2, and no amorphization occurred. This is in contrast to the subsurface damage of hard and brittle materials, such as silicon, where an amorphous layers form immediately below the machined surfaces (Yan et al., 2009). In addition, cutting CaF_2 using a 0° rake angle diamond tool can produce less subsurface damage than that when using a negative rake angle tool. Mizumoto and Kakinuma (2018) investigated the influences of crystallographic orientations on the brittle-to-ductile transition of CaF_2 through several plunge-cut experiments in various cutting directions. They found that material deformation behaviors were mainly determined by primary slip systems $\{100\}< 110 >$, cleavage planes {111}, and partial cleavage planes {110}. Komiya et al. (2018) applied the fly cutting method to fabricate micro-grooves on CaF_2 using diamond tools with square tips for creating sharp edges of the grooves. Micro chippings easily occurred at the edges of the grooves, and a down-cut could achieve a higher critical undeformed chip thickness for ductile-to-brittle transition than in case of an up-cut. Chen et al. (2017a) conducted scratching tests on CaF_2 wafers with different crystal planes and scratched along various crystal orientations using spherical diamond tips to investigate the material removal of CaF_2 related to anisotropy. The maximum critical load for scratching CaF_2 in the ductile mode was achieved on the (111) plane. Chen et al. (2017b) optimized cutting parameters and machined a flat surface on CaF_2 in ductile mode with a surface roughness of 2.8 nm Ra. To enhance ductile-mode machining of CaF_2, Lee et al. (2021) coated CaF_2 workpiece with epoxy resin before the cutting process; Guo et al. (2022b) applied weak magnetic fields in the cutting of CaF_2; and Wang et al. (2016a) cut CaF_2 at elevated temperatures. Plunge-cut experiments were performed using these techniques to validate their effectiveness. Bodlapati et al. (2021) studied the influence of anisotropy on the machining characteristics of CaF_2 via laser-assisted diamond turning and reported that machining the (100) crystal plane resulted in less tool wear than machining the (211) and (111) crystal planes. Moreover, fundamental investigations on the effects of tool geometry (Chen et al., 2012) and crystal anisotropy (Wang et al., 2016b) on material deformation behaviors in diamond cutting CaF_2 were conducted using finite element method (FEM) simulations. Guo et al. (2023) conducted molecular dynamics simulations to reveal the behavior of magnetoplasticity during CaF_2 deformation.

Despite the several attempts to understand the cutting mechanisms and improve the machinability of CaF_2, studies on the cutting of CaF_2 for freeform surfaces are scarce. Zhang et al. (2020b) sculptured a hexagonal microlens array on CaF_2 using an elliptical vibration diamond cutting device that could control the vibration amplitude of tools. However, in this machining process, each lens was created by single-pass cutting without a feed motion perpendicular to the cutting direction. Thus, the parameters of the lenses, such as the diameter and curvature radius of the machined lenses, were only determined by the depth of the cut and tool nose radius. Consequently, the shape flexibility of the lenses is limited. In addition, the machining characteristics in the single-pass cutting of lenses on CaF_2 are yet to be investigated. To machine a freeform microstructured surface of any shape, tool feeding perpendicular to the cutting direction is required to fabricate a tool envelope surface (Zhu et al., 2018). The geometry of chips continuously changes along the direction of tool feeding, and the distance between the finished surface and the critical undeformed chip thickness for generating cracks varies at different tool positions (Yu et al., 2011; Mukaida and Yan, 2017a). Thus, the process of multi-pass cutting to form a tool envelope surface is more complicated than that of single-pass cutting. Till date, there no studies on the fabrication of freeform surfaces on CaF_2 by ultraprecision diamond turning, which generates an envelope of continuous tool-edge profiles in the feed direction. Moreover, the effect of the unique material properties, including low hardness, high brittleness, strong anisotropy, and low thermal conductivity on the machining performance when turning freeform surfaces on CaF_2 remains unclear.

In this study, the fundamental machining characteristics of freeform surfaces on CaF_2 using ultraprecision diamond turning were explored. The surface topography, chip formation, cutting forces, and tool wear were systematically investigated in the cutting experiments of spherical microlens arrays. Optimal conditions for achieving ductile-mode cutting were identified. In addition, a depth-offsetting segment cutting method was proposed to fabricate hexagonal microlens arrays on CaF_2 by preventing crack generation. The results of this study are expected to contribute to the ultraprecision machining of freeform surfaces on CaF_2 and other soft-brittle materials.

2. Experimental procedure

2.1. Experimental setup

The workpiece was a single-crystal calcium fluoride CaF_2 (111) cylinder with a diameter and thickness of 50 and 10 mm, respectively. An ultraprecision machine tool Nanoform X (AMETEK Precitech Inc., USA) that enables simultaneous 4-axis (XZCB) movements was used to fabricate freeform surfaces, as shown in Fig. 1(a). Further, the Z-axis comprised a slow tool servo (STS) system. The workpiece was vacuum-chucked on the workpiece spindle (C-axis). A diamond tool with 0.1 mm nose radius (R), − 20° rake angle, and 28° relief angle was fixed on a tool holder. A piezoelectric dynamometer Kistler 9256C2 was placed below the tool holder to measure the cutting forces during machining. The

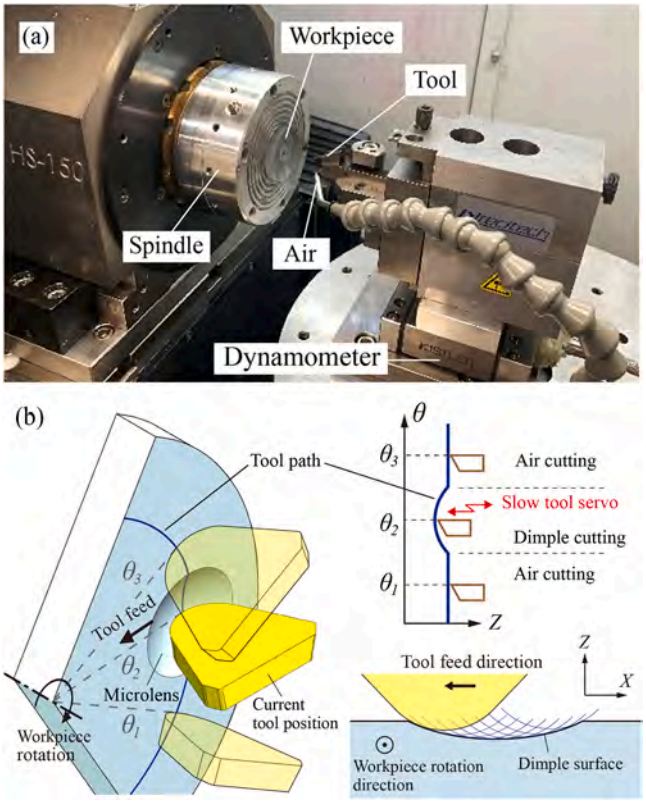

Fig. 1. Experimental setup of diamond turning: (a) photograph of the cutting system, and (b) schematic of the fabrication process of a concave microlens by slow tool servo.

sampling frequency for collecting forces was set to 1 kHz. Before fabricating the microlens arrays, surface flattening was performed on the CaF_2 workpiece to ensure that the workpiece surface was parallel to the X–Y plane of the machine tool. Schematics of the diamond turning of microlenses assisted by the STS system are shown in Fig. 1(b). The rotation of the workpiece spindle was synchronized with the tool feed along the X-axis and the tool servo motion along the Z-axis. In each rotation, the servo movement of the tool along the Z-axis direction was performed to cut the workpieces at varying depths. Meanwhile, the continuous tool feed along the X-axis direction generated an envelope curve to form a complete spherical dimple. Therefore, freeform surfaces can be generated on the workpiece based on a tool-path program containing the X-, Z-, and C-axis coordinates. While cutting the microlenses, the tool only cut the workpiece at the position where a designed lens was present, whereas in other positions, air cutting was performed.

2.2. Fabricating microlens arrays

As a test cut, a spherical microlens array was fabricated on the (111) crystal plane of CaF_2, as shown in Fig. 2(a). The design of the spherical microlens array and the crystal orientation-dependent cutting directions are illustrated in Fig. 2(b). The microlens array comprised 12 dimples designed with a diameter, depth (D), and curvature radius (Rd) of 320 μm, 5 μm, and 2.5625 mm, respectively. These dimples were distributed on a circle with a radius of 1 mm. The angular pitch of the dimples was 30°. When cutting the dimples at angular positions $C = 0°$, 60°, 120°, 180°, 240°, and 300°, the cutting directions were the $< 112 >$ crystallographic directions, and when cutting the dimples at angular positions $C = 30°$, 90°, 150°, 210°, 270°, and 330°, they were $< 110 >$ crystallographic directions.

As another test cut, a hexagonal microlens array was fabricated on the (111) crystal plane of CaF_2. The hexagonal microlens array, with no gaps between the lenses, has the highest ratio of lens area to the total area. A uniform light distribution can be obtained when a point or line light source passes through this microlens array. Thus, hexagonal microlens arrays have wide applications in optics, such as bionic compound eyes (Yang et al., 2018) and Shack-Hartmann wavefront sensors (Zhang et al., 2018). The generation principle of the hexagonal microlens arrays is shown in Fig. 3(a). A central spherical lens is surrounded by six evenly spaced lenses of the same size as the central spherical lens; the surrounding six lenses partially overlap with the central lens to cause the entire edge of the central lens to interfere with these lenses. Consequently, the central lens becomes hexagonal in shape, and other hexagonal lenses can be fabricated in the same manner. Fig. 3(b) shows the design of the hexagonal microlens array and the crystal orientation-dependent cutting directions. Multiple dimples with depth (D) and curvature radius (Rd) of 5 μm and 2.5625 mm, respectively, intersected each other. They formed an array of regular hexagonal lenses, where the length of the side of a hexagon was 160 μm, and the

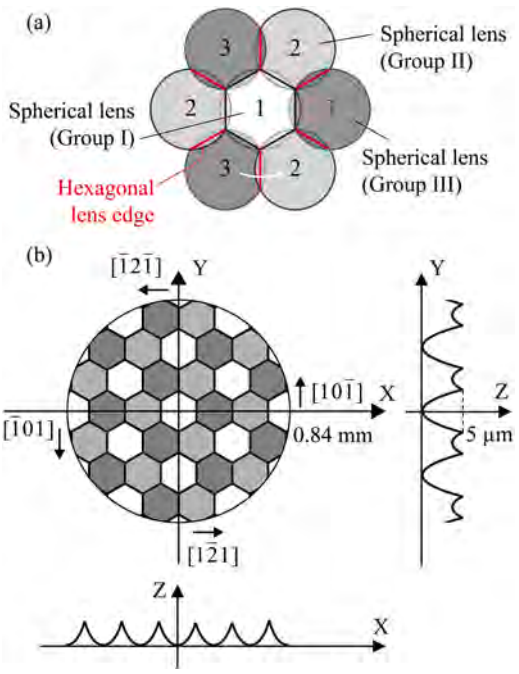

Fig. 3. Schematic of the machining of a hexagonal microlens array: (a) generation principle of a hexagonal microlens, and (b) design parameters of the hexagonal microlens array.

diameter of the array was 1.68 mm. The tool used for cutting the hexagonal microlens array was the same as that used for cutting the spherical microlens array. The experimental conditions of the spherical and hexagonal microlens arrays are summarized in Table 1.

Theoretically, the edge of a hexagonal microlens created by the intersection of two overlapped lenses is very sharp. Such sharp edges are

Table 1
Machining conditions for spherical and hexagonal micro lenses arrays.

Parameters	Value	
Workpiece	CaF_2 (111)	
Cutting tool	Single-crystal diamond	
Nose radius	0.1 mm	
Rake angle α	− 20°	
Relief angle γ	28°	
Cutting parameters	Spherical microlens array	Hexagonal microlens array
Depth of cut d	0 – 5 μm	1 – 6 μm
Feed rate f	0.2, 0.7, 0.9, 1.1 μm/rev	0.2 μm/rev
Spindle rotation speed	25 – 35 rpm	20 rpm
Cutting speed	0.19 m/min	0 – 0.11 m/min
Environment	Dry	

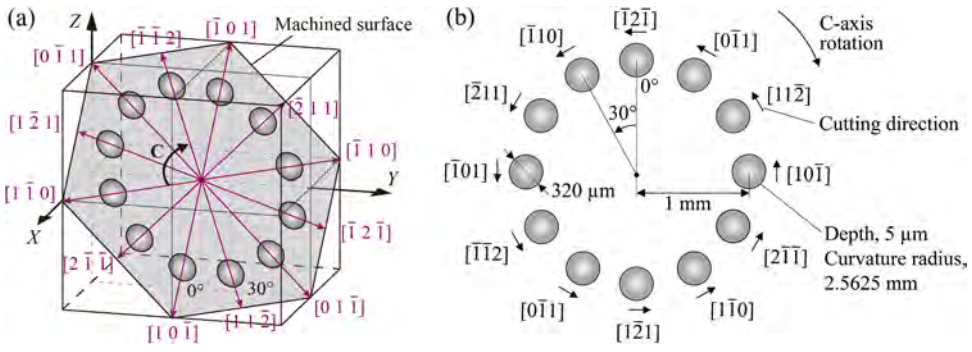

Fig. 2. Schematic of the machining of a spherical microlens array: (a) planar orientation of the machined surface in CaF_2 crystals, and (b) design parameters of the spherical microlens array.

difficult to produce in one step using a continuous toolpath as in the fabrication of spherical microlens arrays. This is because the Z-axis moves with high acceleration, resulting in an increased tool tracking error. As an alternative, the segment cutting method has been used for fabricating sharp edges on various materials, such as silicon (Mukaida and Yan, 2017b) and aluminum alloy (Zhang et al., 2019). The dimples were divided into three non-adjacent groups (groups I, II, and III) for cutting, as shown in Fig. 3(b). In this case, when cutting each group of dimples, the Z-axis acceleration decreased, and its variation became smooth. A hexagonal lens array with sharp edges was fabricated by superimposing the dimples machined by the three groups.

Fig. 4(a) illustrates an example of fabricating a sharp edge along the white arrow line indicated in Fig. 3(a) using the conventional segment cutting method. The apex of the edge formed by the intersection of the two lenses was on the unmachined workpiece surface plane. Thus, the material removal volume and depth of the cut for creating a certain lens array were minimal, thereby reducing tool wear and increasing machining efficiency. However, in this study, in contrast to cutting silicon and aluminum alloy, when cutting CaF_2, cracks were prone to form in the lens edge in the cutting direction. When using the conventional segment cutting method, cracks were formed on the edges of the machined lenses, as shown in Fig. 4(a). To fabricate hexagonal lens arrays with good surface quality on CaF_2, a depth-offsetting segment-cutting method was proposed, as shown in Fig. 4(b). Similar to the conventional segment cutting method, the lenses were divided into non-adjacent groups for cutting. However, the edge of the design surface shifted several microns below the substrate surface. For example, to create a hexagonal lens edge similar to that in Fig. 4(a), Group II spherical lenses can first be fabricated on the substrate surface with a relatively large feed rate, although cracks may form in the cut-in/cut-out regions of the lenses. Owing to the depth offset, the toolpaths for cutting the next group of lenses (i.e., Group III) partially overlapped those of with Group II. Therefore, by machining the lenses of Group III with a low feed rate, crack-free surfaces were obtained in the entire area of Group III lenses. Moreover, the cracks formed in the edges of Group II lenses were also removed.

2.3. Measurement and characterization

The general view of the fabricated microlens arrays was captured via an optical microscope VHX-1000 (Keyence Corp., Japan) and differential interference contrast microscopy (DICM). Subsequently, high-magnification views of the machined lenses, cutting chips, and tool wear were characterized using scanning electron microscopy (SEM). Further, a white light interferometer was used to measure the three-dimensional (3D) topographies of the fabricated microlens arrays.

3. Results and discussion

3.1. Surface topography

Four different feed rates of $f = 0.2$, 0.7, 0.9, and 1.1 μm/rev, were used for machining spherical microlens arrays. Fig. 5(a) and (b) show the full views of the microlens arrays machined at feed rates of 0.2 and 1.1 μm/rev, respectively. In general, when $f = 0.2$ μm/rev, the lenses located on each angle demonstrated good surface quality, as indicated by the surfaces with glossy reflection. In contrast, for $f = 1.1$ μm/rev, brittle fractures were generated in most lenses, resulting in dark surfaces, particularly the lenses located at $C = 60°$ and 300°. Nevertheless, lenses with glossy surfaces can still be generated in certain locations, such as $C = 0°$ and 180°. This result indicates a strong anisotropy of the CaF_2 crystal; in particular, the lenses located at $C = 60°$ and 300° are the most likely to form cracks, thus limiting the machining quality and efficiency.

To further investigate this issue, close-up views of the machined lenses located at $C = 60°$ and 300° at four different feed rates were captured and compared with those of the lenses machined with varied feed rates located at $C = 0°$, as shown in Fig. 6. When machining lenses located at $C = 0°$, crack-free surfaces were obtained at all feed rates. However, when machining the lenses located at $C = 60°$ and 300°, brittle fractures were initiated at the edges of the lenses when the feed rate increased from 0.2 to 0.7 μm/rev. With further increase in the feed rate, brittle fractures extended to the entire lens. Notably, brittle fractures tended to form first at the cut-in and cut-out regions, and the range of the surface damage increased along the cutting direction with increase in the depth of cut. Moreover, the extent and degree of surface defects at the edges of the cut-in region were more significant than those of the cut-out region.

To observe the surface defects in the edges of the cut-in and cut-out regions in more detail, the edges of the lens machined with a feed rate of 0.2 μm/rev located at $C = 300°$ were captured by SEM, as shown in Fig. 7. In the cut-in region (Fig. 7(a)), the surface defects were dominated by clusters of submicron pits. In addition, a few craters with an approximate size of 1 μm appeared in the cluster of pits. However, in the cut-out region (Fig. 7(b)), no surface defects were formed. Although certain submicron pits were generated in the cut-in region, from a macro perspective, these defects exerted minimal effect on the optics, as proven by the optical microscope image of the lens ($f = 0.2$ μm/rev, $C = 300°$) presented in Fig. 6. However, when the feed rate increased to 0.7 μm/rev, greater μm-scale craters began to form in the cut-in region, as shown

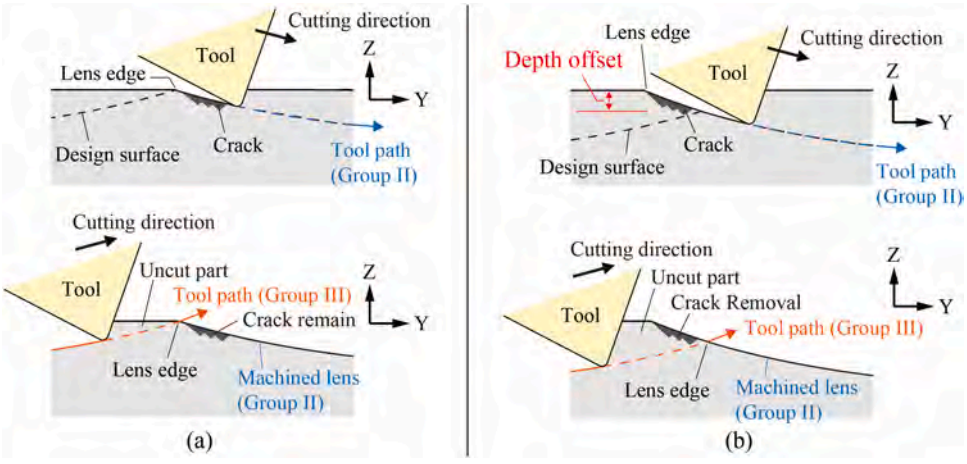

Fig. 4. Schematic of the toolpath when cutting hexagonal microlens arrays using: (a) conventional segment cutting, and (b) depth-offsetting segment cutting methods.

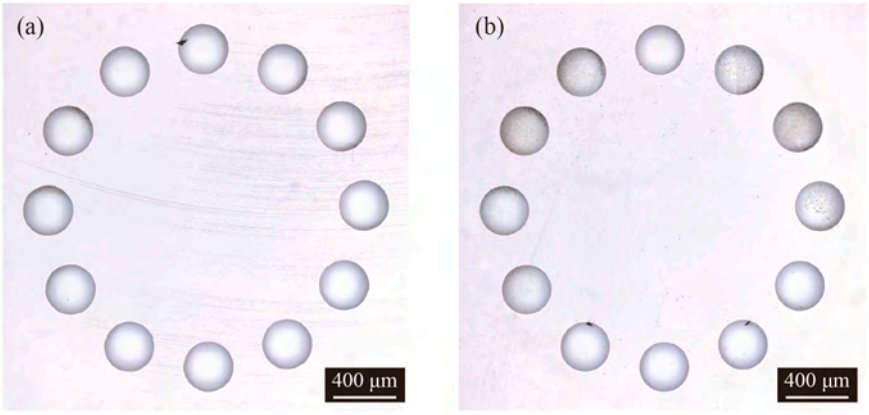

Fig. 5. Optical microscope images of circular microlens array machined on CaF_2 with different feed rates: (a) $f = 0.2$ μm/rev, and (b) $f = 1.1$ μm/rev.

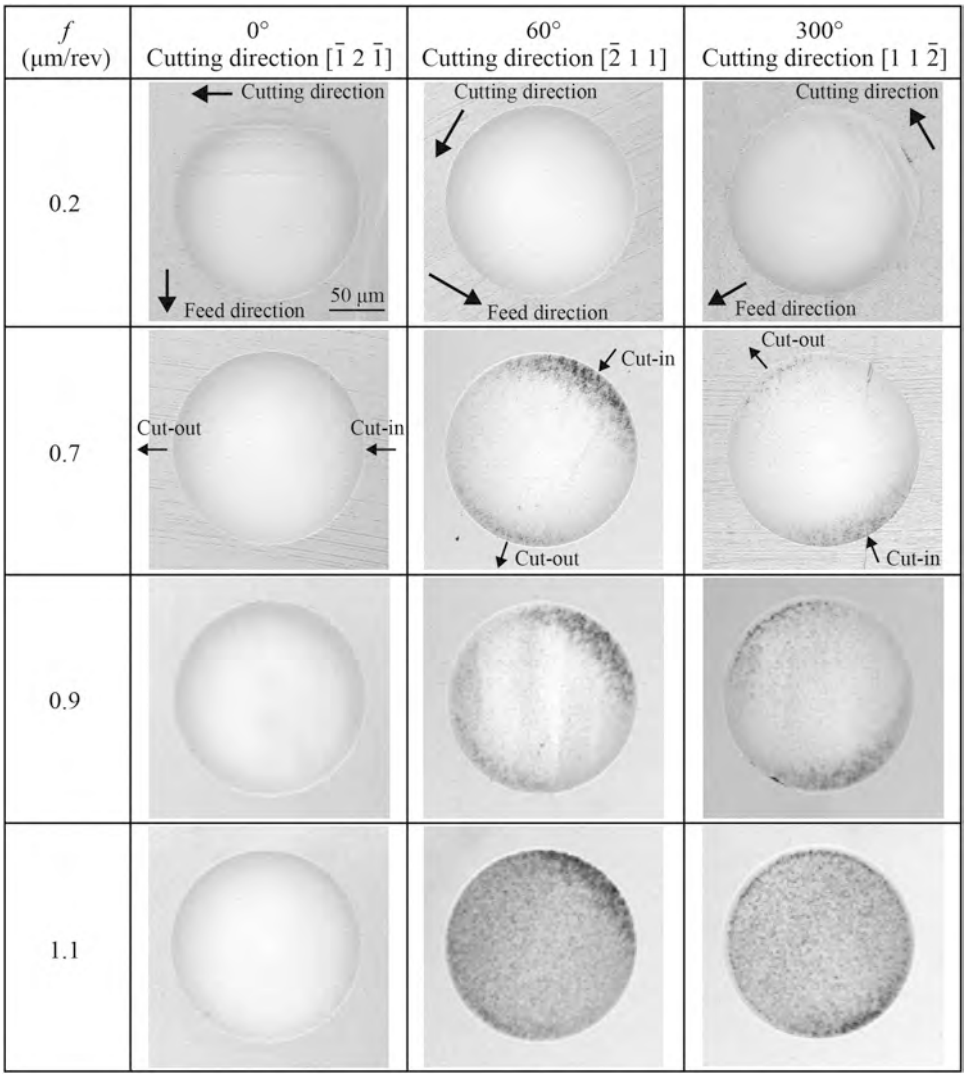

Fig. 6. Optical microscope images of lenses machined along different cutting directions with various tool feed rates.

in Fig. 8(a). These craters decreased the optical performance, as indicated by the optical microscope image of the lens where dark spots appeared in the cut-in region ($f = 0.7$ μm/rev, $C = 300°$ in Fig. 6). With further increase in the feed rate to 0.9 and 1.1 μm/rev, the size of the craters increased, and the range of surface damages expanded, as presented in Fig. 8(b) and (c). Therefore, multiple dark spots were observed on these lenses ($f = 0.9$ and 1.1 μm/rev, $C = 300°$ in Fig. 6) via optical microscopy, and the edges of the cut-in region appeared black owing to the generation of dense and large craters.

The 3D topography and surface roughness of the lenses were measured using a white light interferometer. Fig. 9 shows plots of the 3D topography of the lenses located at $C = 0°$ and 300°, machined at 0.2

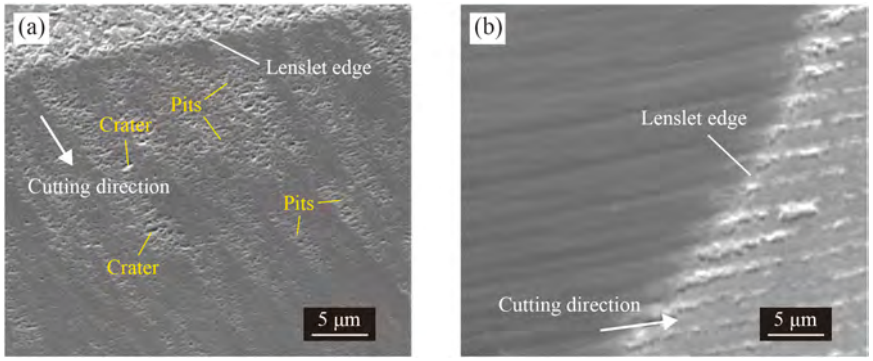

Fig. 7. SEM images of (a) cut-in region, and (b) cut-out region of a lens. ($f = 0.2$ μm/rev; $C = 300°$).

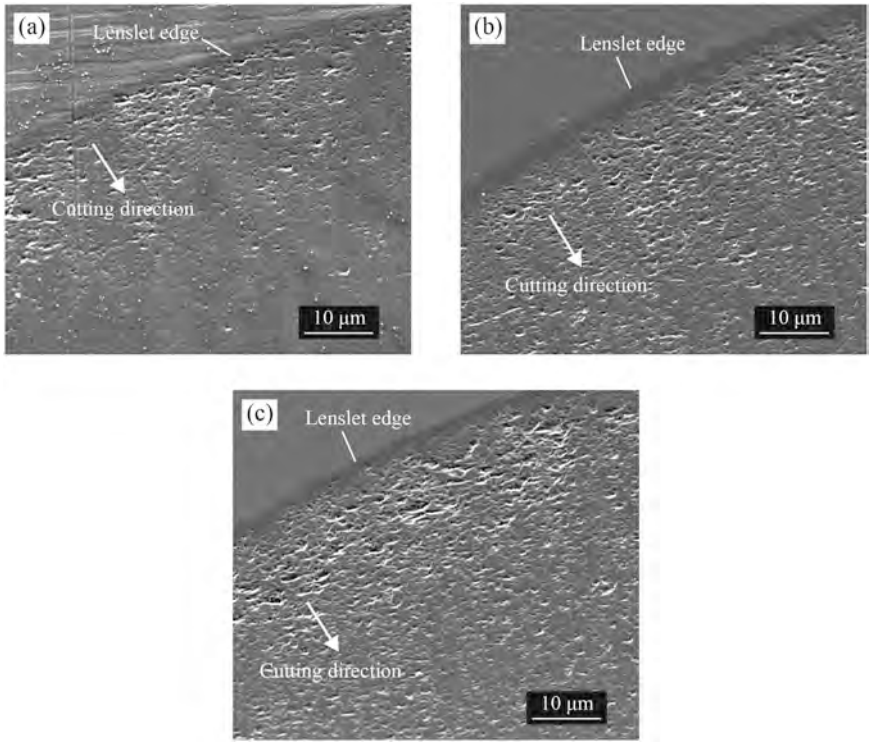

Fig. 8. SEM images of the edges of the cut-in region for the lenses located on $C = 300°$ with feed rates of (a) 0.7, (b) 0.9, and (c) 1.1 μm/rev.

and 1.1 μm/rev feed rates. At $f = 0.2$ μm/rev, lenses with smooth surfaces were created at $C = 0°$ and 300°; whereas, at $f = 1.1$ μm/rev, although the lens located at $C = 0°$ exhibited a smooth surface, several brittle fracture-induced noise spikes appeared on the lens located at $C = 300°$. The surface roughness was calculated after removing the ideal shape from the measured topography within a radius of 155 μm from the center of the lens (excluding the lens edge). The standard roughness parameters of the lenses, including the mean roughness (Sa) and root mean square of roughness (Sq), are indicated accordingly in Fig. 9.

Fig. 10 shows the roughness of the lens surfaces fabricated under varied feed rates at different angles. When the feed rate was 0.2 μm/rev, all lenses were machined in the ductile mode. This is because at a sufficiently small feed rate, the undeformed chip thickness was below the critical values for brittle fracture in all crystal directions. Thus, the roughness of the lenses at each orientation angle was small, and the values were similar, resulting in a circular plot. However, with increasing feed rate, the anisotropy of the crystal became apparent because the undeformed chip thickness gradually increased and exceeded the critical values for brittle fracture in certain directions. Consequently, brittle fractures occurred along those directions, causing a significant increase in the surface roughness. This resulted in propeller-like surface roughness plots.

The plastic deformation of single-crystal CaF_2 tends to occur in $\{100\}<110>$ slip systems, and brittle fractures of the material are prone to occur in the {111} cleavage planes. However, owing to the softness of CaF_2, slip mobility exerts a greater influence than cleavage mobility on the brittle-to-ductile transition mechanism (Mizumoto and Kakinuma, 2018). Therefore, the plastic deformation factor P, which estimates the probability of activating the primary slip systems $\{100\}<110>$, can be used to predict the variation trend of the critical undeformed chip thickness with crystal orientation. Consequently, the trends in surface roughness resulting from different cutting directions can be predicted. The larger the value of P, the greater the critical undeformed chip thickness and the smaller the surface roughness. The plastic deformation factor P can be expressed as follows (Mizumoto and Kakinuma, 2018):

$$P = \frac{m}{\tau_{CR}/\min \tau_{CR}} \tag{1}$$

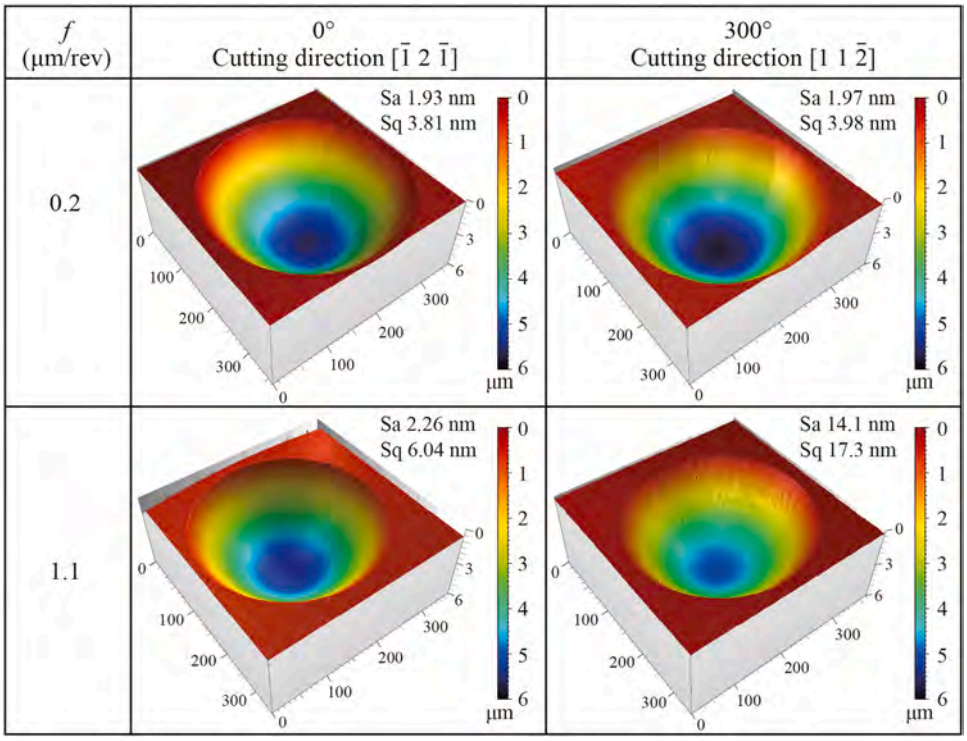

Fig. 9. 3D topographies of lenses machined along different cutting directions with various tool feed rates.

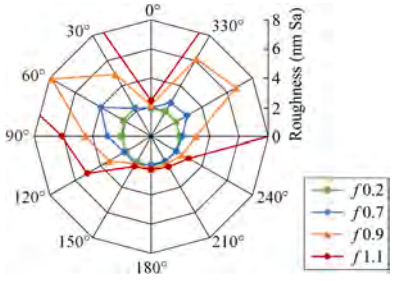

Fig. 10. Roughness of the lenses surfaces fabricated under varied feed rates on different angles.

where m and τ_{CR} are the Schmid factor and critical resolved shear stress for the primary slip systems, respectively, and min τ_{CR} is the minimum critical resolved shear stress in the total slip systems of CaF_2.

When the workpiece rotated and the tool cut the lenses located at $C = 300°$, 0°, and 60° in sequence, the cutting directions were perpendicular to the position directions of the lenses and coincided along the [11 − 2], [− 12 − 1], and [− 211] crystal directions, respectively. According to Mizumoto and Kakinuma (2018), the plastic deformation factor P is a minimum when cutting along the [11 − 2] direction, and is a maximum when the cutting direction changes to [− 12 − 1]. Subsequently, P returns to a minimum when the cutting direction changes to [− 211]. Therefore, the lenses located at $C = 60°$ and 300° are predicted to have the largest surface roughness, and those located at $C = 0°$ has the smallest value, which is consistent with the experimental results shown in Fig. 10. Notably, according to Yan et al. (2003) and Mizumoto and Kakinuma (2018), the CaF_2 (111) plane exhibits a three-fold symmetry in the plastic deformation factor and critical undeformed chip thickness, that is, the surface roughness of the lens located at $C = 180°$ should also be the largest. However, the results depicted in Fig. 10 show that the surface roughness of the lens at $C = 180°$ was much smaller than that of the lenses at $C = 60°$ and 300°. This inconsistency may be attributed to the surface flattening performed before cutting the lenses, which generated certain defects in the subsurface of the crystal, thereby affecting the symmetry of the machining characteristics of the crystal.

In general, the required surface roughness of optical components is determined by the extent of the tolerable scatter loss. Harvey et al. (2012) proposed an evaluation parameter of total integrated scattering (TIS) and defined it as follows:

$$\mathrm{TIS} \approx \left(\frac{4\pi\delta}{\lambda}\right)^2 \tag{2}$$

where δ is Sq and λ is the wavelength of the incident radiation. Typically, TIS should be smaller than 1% for most optical systems (Mukaida and Yan, 2017a). When fabricating a spherical microlens array on CaF_2 at $f = 0.2$ μm/rev, the surface roughness was barely affected by material anisotropy. As maximum Sq of 3.98 nm in the lens is at $C = 300°$, the entire microlens array is qualified as an optical surface for $\lambda > 0.5$ μm. Considering that CaF_2 lenses are primarily used as optical parts in 0.25–7.0 μm wavelength range, the spherical microlens array machined at $f = 0.2$ μm/rev can satisfy the requirement at wavelengths that cover 96.3% range of the transmission spectrum of CaF_2.

3.2. Cutting chips morphology

To clarify the material removal behavior at various feed rates, SEM images of the cutting chips collected during machining are shown in Fig. 11. When the feed rate was 0.2 μm/rev, continuous ribbon-like chips were generated, as shown in Fig. 11(a). This implies that the cutting process was performed in the ductile mode. The material was removed via stable shear and/or extrusion deformation, resulting in uniform and crack-free surfaces on all lenses. When increasing the feed rate to 0.7 μm/rev, a mixture of ribbons-like and powder-like chips was formed, as shown in Fig. 11(b). This is because, on the one hand, the critical undeformed chip thickness (h_c) for ductile to brittle mode transition varied in the machining of lenses with different angles owing to crystal anisotropy. On the other hand, in cutting a certain lens, the maximum undeformed chip thickness (h_m) changed with the cutting position in the lens, as illustrated in Fig. 12. The maximum undeformed

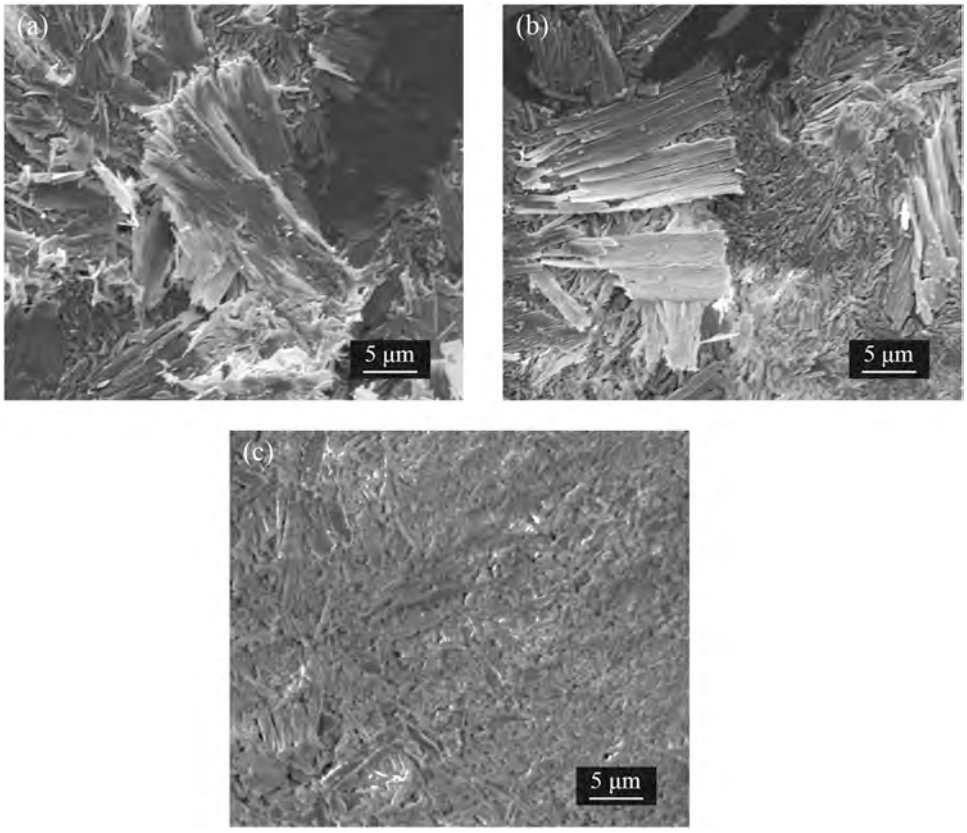

Fig. 11. SEM images of cutting chips generated at the feed rates of (a) 0.2, (b) 0.7, and (c) 1.1 μm/rev.

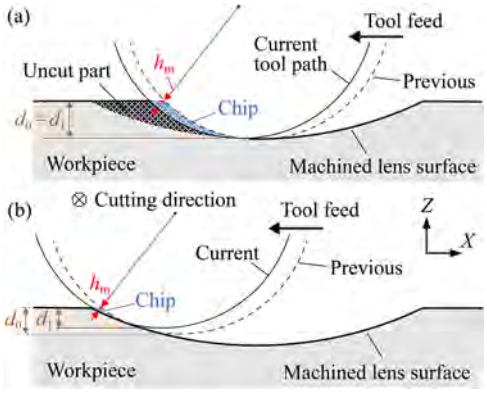

Fig. 12. Schematics of the undeformed chip cross-section in the lens machining when the tool feeds to (a) lens center, and (b) lens edge.

thickness corresponding to any position of the tool during lens cutting can be calculated using Eq. (3), according to Mukaida and Yan (2017a):

$$h_m = R - \sqrt{x^2 + (R - d_1)^2} \tag{3}$$

where $x = \sqrt{R^2 - (R - d_0)^2} - f$, R is the tool nose radius, d_0 and d_1 are the depth of cut for the previous and current tool paths, respectively, f is the tool feed rate along the X-axis.

Fig. 13(a) plots the variation of h_m in the cross section parallel with the direction of tool feeding when cutting the bottom of the lens with f = 0.2 μm/rev. The cross section of the lens and tool path are indicated by black and dark blue lines, respectively. Because the tool has a nose radius, the tool path planning must be compensated to improve the form accuracy of freeform surfaces (Yu et al., 2012). This causes a slight deviation in the tool path from the lens profile, particularly at the lens edges. When the tool continuously feeds from right to left to fabricate a lens, the h_m increases rapidly at first and reaches a maximum before the tool feeds to the center of the lens. Thereafter, the h_m gradually decreases to zero as the tool continues to feed to the left. The h_m in cutting a lens at f = 0.2 μm/rev is approximately 60 nm, which is lower than the h_c for ductile to brittle mode transition of any crystal direction on (111) CaF_2, according to Mizumoto and Kakinuma (2018). At such nanometric scale, the material was plastically deformed by shearing and/or extrusion similar to the nano-cutting of other brittle materials (Fang et al., 2005). Consequently, chips were formed in continuous ribbon shape, as shown in Fig. 11(a). Therefore, when f = 0.2 μm/rev, all lenses located at different angles were machined in ductile mode. Fig. 13(b) compares the h_m at various feed rates. Here, h_m increased with increasing feed rate. When f = 0.7 μm/rev, the h_m reached > 200 nm, which is larger than the h_c of certain crystal directions, such as the directions for cutting the lenses at C = 60 and 300°. Consequently, part of the chips was generated in brittle mode, as shown in Fig. 11(b). When f = 1.1 μm/rev, h_m reached approximately 350 nm, which is larger than the h_c of most crystal directions. Thus, brittle-mode chip formation became dominant, and the cutting chips were generated primarily in the form of powder, as shown in Fig. 11(c).

3.3. Cutting force

The cutting forces were also measured during the machining of the spherical microlens array. Fig. 14 shows the curves of the principal (F_c) and thrust (F_t) forces in real time during one revolution of the workpiece when the tool passed the center of lenses at f = 0.2, 1.1 μm/rev. In general, the principal and thrust forces under both feed rates display a periodic variation. They are characterized by an increase from zero to a peak, and then a decrease to zero. Considering that the spindle rotated at approximately 30 rpm when the tool was fed towards the lens center,

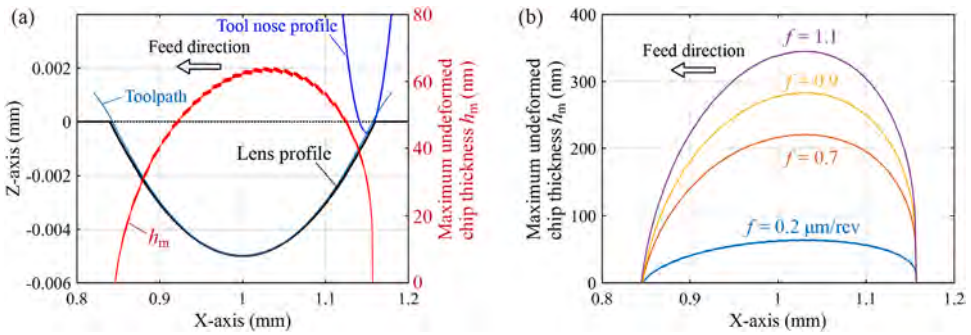

Fig. 13. (a) Variation of maximum undeformed chip thickness in feed direction when cutting lenses at $f = 0.2$ μm/rev. (b) Comparison of maximum undeformed chip thickness at varied feed rates.

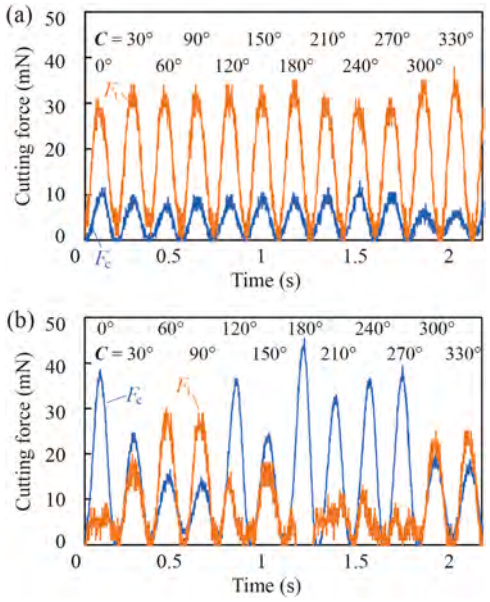

Fig. 14. Real time curves of the principal force (F_c) and thrust force (F_t) under the feed rates of (a) 0.2, and (b) 1.1 μm/rev.

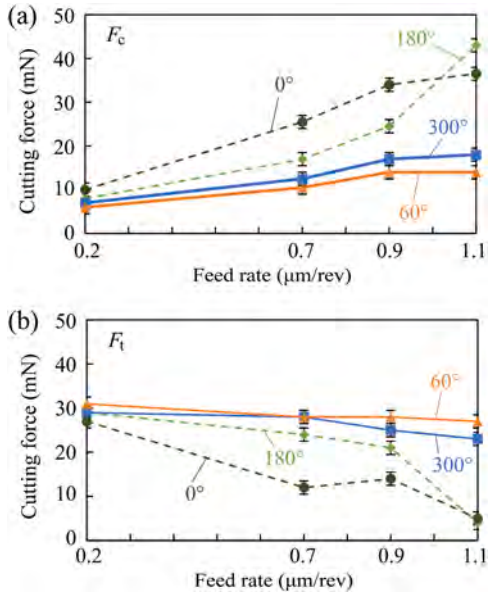

Fig. 15. Peak values of (a) principal force (F_c), and (b) thrust force (F_t) in the machining of lenses with different angles at varied feed rates.

the cutting time from the center of one lens to the center of the next lens was approximately 0.165 s. This time coincides with the time between the peaks of the cutting forces in two adjacent waves. This indicates that each wave of the cutting forces corresponds to one lens cut, and the variation trend of the cutting forces is consistent with that of the depth of cut.

When the feed rate was 0.2 μm/rev, the peak principal and thrust forces generated by each lens cut were nearly constant, as plotted in Fig. 14(a). In addition, F_t was much larger than F_c. This is attributed to the small contact area between the tool and workpiece along the cutting direction, leading to a small principal force. On the other hand, the tool not only moved forward but pressed into the workpiece in the depth direction, similar to indentation processes. This caused a large thrust force. When the feed rate to 1.1 μm/rev, the peak cutting forces generated during each lens cut fluctuated, as shown in Fig. 14(b). The principal force at $f = 1.1$ μm/rev was significantly increased compared with that at $f = 0.2$ μm/rev, owing to an increased tool-workpiece contact area. In contrast, the thrust force decreased, and its wave shape became irregular. This may be attributed to the interference of brittle fractures that occurred at large feed rates with the force measurement; in particular, the initiation of cracks on the machined surface suddenly reduced the force acting on the tool by the workpiece. The peak principal and thrust forces in the cutting of typical lenses located at $C = 0°$, 60°, 180°, and 300° with varied feed rates are plotted in Fig. 15. A general trend was observed wherein the peak principal forces increased with increasing feed rate. In contrast, the peak thrust force decreased with increasing feed rate, independent of the lens location.

3.4. Tool wear

After cutting the microlenses on CaF_2 for a cutting distance of approximately 50 m, tool wear was observed by SEM, as shown in Fig. 16(a). Although certain chips adhered to the tool rake face, no chipping occurred on the cutting edge, even without any obvious wear on the rake or flank face of the tool. This is in contrast to the tool wear after cutting lenses on silicon, wherein microchipping and flank wear were observed after a short cutting distance of approximately 0.5 m (Mukaida and Yan, 2017a). The insignificance of tool wear in cutting CaF_2 was considered attributed to its low hardness of approximately 1.8 GPa (Mizumoto et al., 2011). In contrast, the hardness of silicon is approximately 10 GPa (Leung et al., 1998).

To characterize the forms of tool wear after cutting CaF_2 for a long distance, a flat face turning test for a cutting distance of approximately 5000 m was performed on CaF_2 using the same tool at a cutting depth of 2 μm, feed rate of 2 μm/rev, and spindle speed of 1000 rpm. Fig. 16(b) shows the tool wear after the flat face turning test. Clear crater wear was observed in the rake face of the tool; however, the wear in the flank face was insignificant. In addition, the shape of the crater wear was similar to

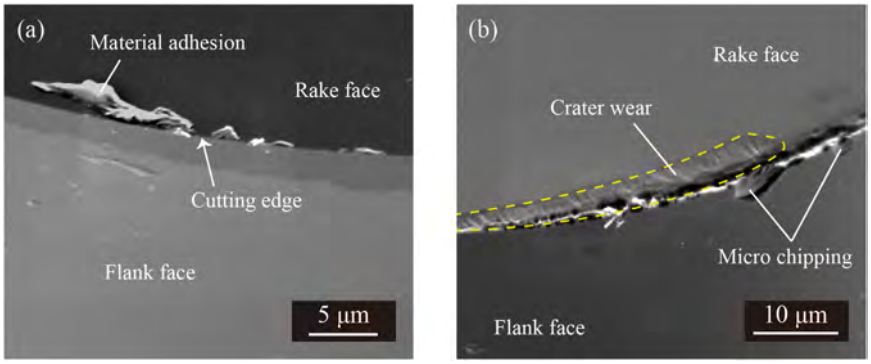

Fig. 16. SEM images of tool edges after (a) cutting a circular microlens array (cutting distance of approximately 50 m) and (b) cutting a flat plane (cutting distance of approximately 5 km).

that of the undeformed chip when cutting the surface with round-nose tools, as shown in Fig. 17(a). This implies that the friction between the undeformed chips and the tool rake face was the main cause of crater wear. When cutting CaF_2 under dry conditions, most of the cutting heat was generated in the primary deformation zone owing to material deformation and could not be cooled down. Owing to the extremely low thermal conductivity of CaF_2, it was difficult to dissipate the heat to the substrate; however, it was carried away by the chips. Therefore, the friction between the high-temperature chips and the tool rake face resulted in crater wear in the rake face, as shown in Fig. 17(b). Despite friction at the workpiece-tool flank face interface, flank wear was not obvious because the hardness of CaF_2 was much lower than that of the diamond tool. In addition, the temperature in this friction zone was relatively low. Microchipping was also observed on the cutting edge near the maximum undeformed chip thickness. The large undeformed chip thickness and the unstable tool-workpiece contact when cutting materials in brittle mode may have caused the microchipping.

3.5. Discussion on crack formation mechanisms

When cutting microlens arrays on CaF_2, under a large feed rate, cracks were easily formed at the edges where the tool cut in and cut out the workpiece in the cutting direction. In addition, the cracks were more pronounced in the cut-in region than in the cut-out region. The principal and thrust force variations when cutting a single lens are extracted from Fig. 14(a) and are plotted in Fig. 18 (a). To remove the noise from the force signals, a seventh-order polynomial was used to fit the original force curve, which is plotted in Fig. 18(a). The thrust forces reached their peaks before the principal forces reached theirs. To quantify the direction of the resultant force, a force angle β is defined as the angle between the resultant force and F_c, as shown in Fig. 18(b), and can be expressed as

$$\beta = \arctan\left(\frac{F_t}{F_c}\right) \tag{4}$$

The variation in the force angle with the position of the tool is plotted in Fig. 18(a). In general, a large force angle was obtained when the tool cut into the workpiece, and as the tool moved from the cutting-in to cutting-out regions in the cutting direction, the force angle gradually decreased. This indicates that the thrust force was dominant in the cut-in region, and the dominance of the thrust force gradually declined as the tool moved to the cut-out region. Therefore, it is considered that a large tensile stress was generated in the cut-in region caused by the thrust force-induced friction along the direction of cutting. This resulted in crack formation after the tool passed the cut-in region of the lenses, as shown in Fig. 18(b). In contrast, the thrust force-induced friction decreased in the cut-out region, leading to reduced tensile stress. However, the hydrostatic pressure, which enhances the ductile mode cutting (Yoshino et al., 2001), was decreased in the cut-out region owing to the lack of material behind the cut-out region to resist the tool movement to maintain a high hydrostatic pressure at the tool-workpiece contact areas. Thus, cracks can be generated in front of the tool when cutting the cut-out region of the lenses, as shown in Fig. 18(c). Lee et al. (2019) applied a solidified layer on the CaF_2 surface to increase the hydrostatic pressure in the cutting area and enhance the ductile mode cutting of CaF_2. This can prove that the lack of hydrostatic pressure when the tool cuts out lenses is the primary reason for crack formation in the cut-out region. Notably, microcracks did not occur in the cut-in and cut-out regions of the lenses during the cutting of lenses on silicon. This may be owing to the formation of an amorphous layer during silicon cutting, which improved the ductile machinability (Mukaida and Yan, 2017a). However, an amorphous layer is not generated in the machined surface of CaF_2 with diamond cutting. Instead, the primary subsurface damages are dislocations and grain refinement, which has been confirmed by (Kakinuma et al., 2015; Mizumoto et al., 2017; Lee et al., 2019). Moreover, the lack of amorphization in the material ensured that the strong fracture toughness anisotropy of CaF_2 were retained. In particular, the maximum critical undeformed chip thickness reached up to approximately 390 nm when cutting along directions such as the [− 12 − 1] crystal direction, whereas the minimum critical undeformed chip thickness was approximately 70 nm when cutting along the crystal directions of [− 211] and [11 − 2] (Yan et al., 2003; Mizumoto and

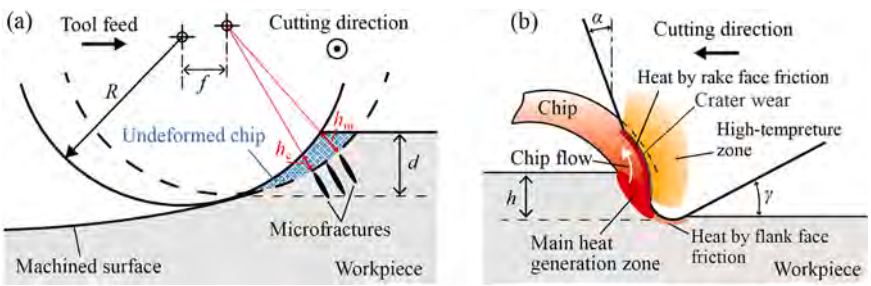

Fig. 17. Schematic models of (a) undeformed chip under the cutting with a round-nosed tool, (b) formation of crater wear in tool rake face.

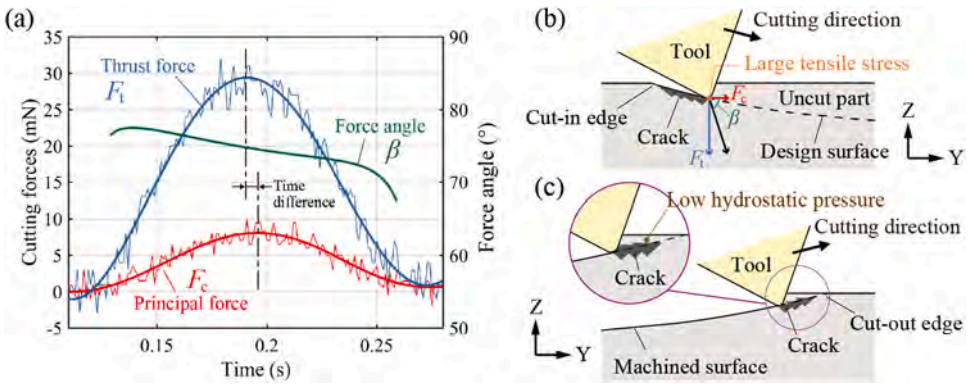

Fig. 18. (a) Variations in cutting forces and force angles in machining lenses with $f = 0.2$ μm/rev. (b) and (c) are schematics of crack generation at the cut-in and cut-out regions, respectively.

Kakinuma, 2018). Therefore, a crack-free surface was obtained at the lens at $C = 0°$ (corresponding cutting direction is [−12 −1]) even when the tool feed rate increased from 0.2 to 1.1 μm/rev. However, cracks were formed in the lenses at $C = 60°$ and 300° (corresponding to cutting directions of [−211] and [11 −2], respectively) once the tool feed rate exceeded 0.2 μm/rev.

3.6. Hexagonal microlens array fabrication

To fabricate a hexagonal microlens array, the machined area must be fully filled with partially overlapping spherical dimples. This indicates that the entire surface structure is cut in all directions in a range of 360°, owing to the characteristics of the diamond turning process. According to the findings in the cutting of spherical lenses, although the cutting direction significantly affects the morphology and quality of the machined surface, a uniformly smooth surface can be achieved by reducing the tool feed rate below a critical value. This ensures that the undeformed chip thickness is smaller than the critical undeformed chip thickness in case of the most difficult-to-cut direction. Therefore, a hexagonal microlens array was fabricated with $f = 0.2$ μm/rev. Fig. 19 shows a DICM image of a hexagonal microlens array fabricated using the depth-offsetting segment cutting method. As evident, the entire surface of every hexagonal lens was free of cracks and had sharp edges. As discussed in Section 3.1, the lens located along the angular direction of $C = 0°$ tended to form a crack-free surface, whereas the lens located along the angular direction of $C = 300°$ easily formed a cracked surface. Therefore, close-up views of the machined surfaces of lenses A ($C = 0°$) and B ($C = 300°$), indicated in Fig. 19, were captured using a confocal laser scanning microscope. Fig. 20 presents a comparison of the center and edge areas of these lenses. As evident. at the center of the lenses, both lenses A and B obtained crack-free surfaces, whereas at the edge of the lenses, a very narrow area of cracks was likely to form, particularly

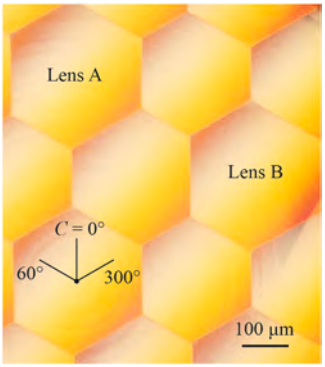

Fig. 19. DICM image of hexagonal microlens array machined on CaF_2.

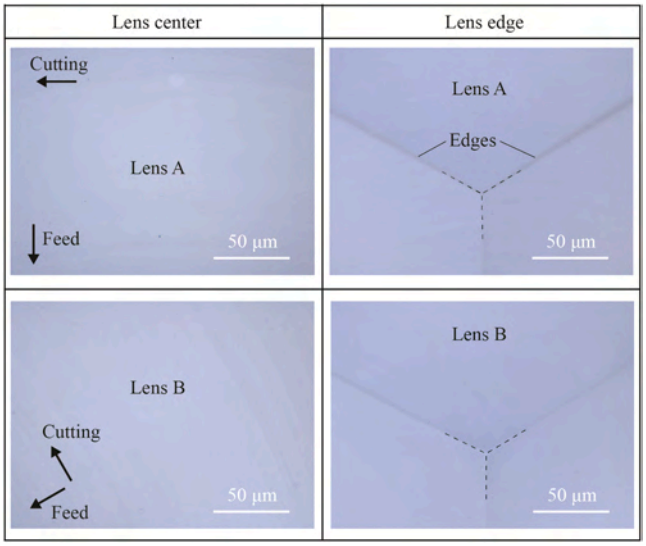

Fig. 20. Confocal laser scanning microscopy images of the machined hexagonal lenses at different positions.

in lens A. This is because when creating the two edges of lens A, the cutting direction approached the [− 211] and [11 − 2] crystal directions.

The 3D topographies of lenses A and B were measured. A general view of the complete lenses and close-up views of the lens edges are shown in Fig. 21. Sharp edges were clearly observed in every lens, thus confirming the effectiveness of using the depth-offsetting segment cutting method to create a hexagonal microlens array with sharp edges on CaF_2. The form errors of the lenses are also presented in Fig. 21. For the two lenses, the peak to valley (P–V) form error calculated over a diameter range of 300 μm excluding the edges was 147 (± 4) nm P–V, and the surface roughness was 4.1 (± 0.1) nm Sa. Mukaida and Yan (2017b) reported cutting a similar hexagonal lens array on silicon with a form error of approximately 300 nm P–V. The form error of the lens fabricated on CaF_2 was smaller than that of the lens fabricated on silicon. This may be attributed to the low hardness of CaF_2 resulting in a relatively low tool wear. However, the fabrication of crack-free lenses on CaF_2 is much more challenging than on silicon because the amorphous phase, which can reduce material anisotropy and promote ductile-mode machining, does not form in the subsurface of CaF_2 during cutting; in other words, the actual brittleness of CaF_2 is higher than that of silicon.

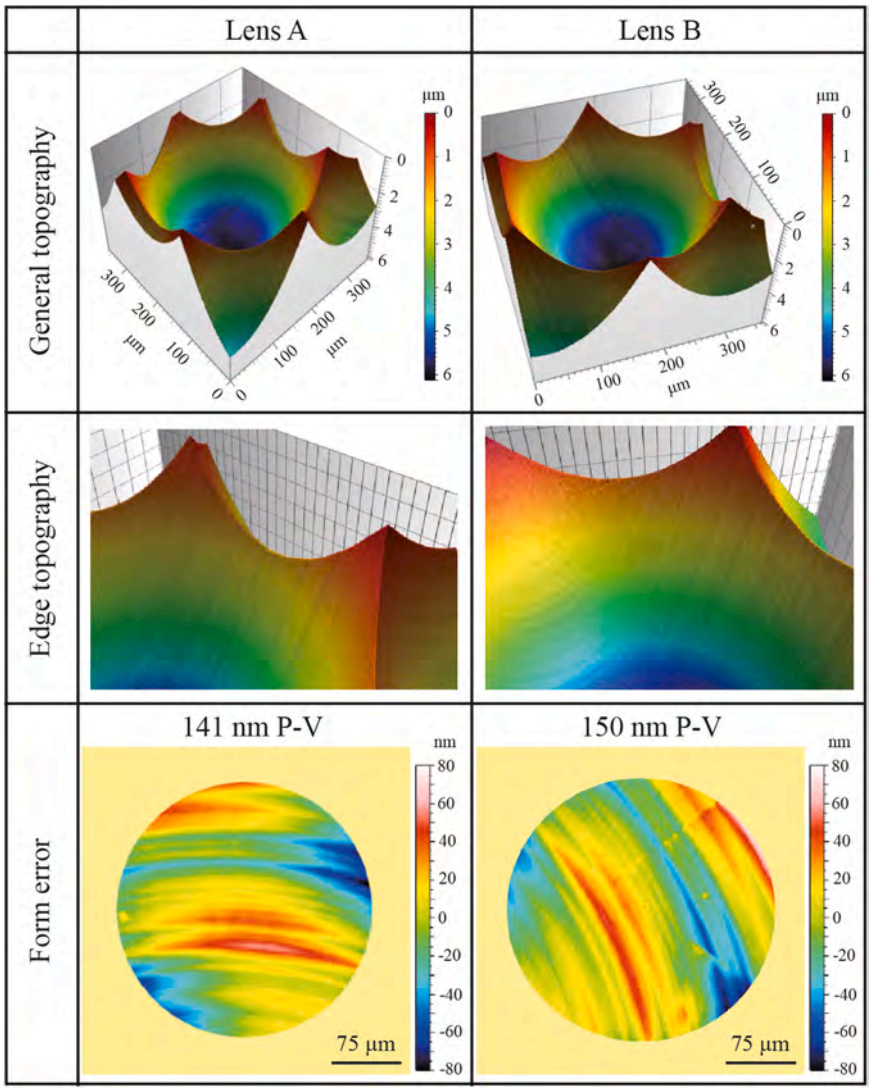

Fig. 21. 3D topography and form error of the machined hexagonal lenses at different positions.

4. Conclusions

This study machined spherical microlenses at various orientations of single-crystal CaF_2 (111) cylinders via diamond turning. The machining characteristics, surface damage formation mechanisms, and tool wear were systematically investigated. Further, a depth-offsetting segment cutting method was proposed to fabricate a hexagonal microlens array with sharp edges. The main conclusions are as follows:

(1) Significant anisotropy was observed when cutting CaF_2. Microcracks were easily formed on the machined surface when cutting along the [− 211] and [11 − 2] crystal directions. In a specific lens, cracks tended to form in the cut-in/cut-out regions along the cutting direction.
(2) Cracks were formed in the cut-in regions of the lenses owing to a large friction-induced tensile stress in the cutting direction because of a large thrust force. In contrast, cracks were formed in the cut-out regions of the lenses owing to the reduced hydrostatic pressure in the material in front of the tool.
(3) During lens cutting, with increase in the cutting depth from zero to the maximum, followed by the subsequent decrease to zero, the principal and thrust forces exhibited the same change trend as that of the cutting depth. However, the thrust forces reached their maximum prior to the principal forces, causing the force angles between the principal and resultant forces to gradually decrease. The peak thrust force decreased with increasing feed rates because the occurrence of brittle fracture in the material became more apparent.
(4) Tool wear was insignificant until a cutting distance of approximately 50 m. When the cutting distance increased to approximately 5000 m, crater wear occurred on the tool rake face and microchipping occurred on the tool cutting edge.
(5) A spherical microlens array, composed of 12 equally spaced lenses lying on the circumference of a circle, was successfully fabricated in ductile mode by controlling the maximum undeformed chip thickness below approximately 60 nm. Material anisotropy exerted minimal influence on the surface roughness of these lenses. The surface roughness was approximately 2 nm Sa.
(6) The depth-offsetting segment cutting method produced a hexagonal microlens array with sharp edges and crack-free surfaces. The surface roughness of the lenses was 4.1 (± 0.1) nm Sa, with form error of 147 (± 4) nm P–V.

The feasibility of fabricating ultraprecision freeform surfaces on CaF_2 via diamond turning was demonstrated. Because CaF_2 is soft and brittle, developing technologies to increase the hydrostatic pressure in the cut-out region of microstructures is beneficial for obtaining good surface quality. In addition, the application of cutting fluids may reduce the

friction between the tool and workpiece and promote heat dissipation from the tool-workpiece interface, resulting in a better surface finish in the cut-in region of the microstructures and smaller crater wear of the tools. However, the potential risk to the use of cutting fluid in causing large surface cracks owing to the high thermal expansion coefficient of CaF_2 should also be considered.

CRediT authorship contribution statement

Weihai Huang: Data curation, Methodology, Investigation, Writing- Original draft preparation. **Kodai Nagayama**: Data curation, Investigation, Writing- Original draft preparation. **Jiwang Yan**: Conceptualization, Methodology, Supervision, Writing- Reviewing and Editing.

Declaration of Competing Interest

The authors declare that they have no known competing financial interests or personal relationships that could have appeared to influence the work reported in this paper.

Data Availability

Data will be made available on request.

References

Bodlapati, C., Kang, D., Navare, J., Turnbull, R., Zhong, Y., Shahinian, H., 2021. Cutting performance of laser assisted diamond turning of calciumfluoride with different crystal orientations. Appl. Opt. 60, 2465–2470.

Chen, L., Hu, L., Xiao, C., Qi, Y., Yu, B., Qian, L., 2017a. Effect of crystallographic orientation on mechanical removal of CaF2. Wear 376–377, 409–416.

Chen, M.J., Xiao, G.B., Li, D., Wu, C.Y., 2012. Multiscale modeling study on the nanometric cutting process of CaF2. Key Eng. Mater. 516, 13–18.

Chen, X., Xu, J., Fang, H., Tian, R., 2017b. Influence of cutting parameters on the ductile-brittle transition of single-crystal calcium fluoride during ultra-precision cutting. Int. J. Adv. Manuf. Technol. 89, 219–225.

Chen, Y., Sun, L., Wu, Y., 2022. Improving the machining performance in single-point diamond turning of curved Zerodur optics by using straight-nosed cutting tools. J. Mater. Process. Technol. 310, 117777.

Fang, F.Z., Wu, H., Liu, Y.C., 2005. Modelling and experimental investigation on nanometric cutting of monocrystalline silicon. Int. J. Mach. Tools Manuf. 45, 1681–1686.

Guo, Y., Yang, X., Kang, J., Zhang, W., Wang, X., Li, M., Wang, Y., Xie, Q., Luo, S., 2022a. Ductile machining of single-crystal germanium for freeform surfaces diamond turning based on a long-stroke fast tool servo. J. Manuf. Process. 82, 615–627.

Guo, Y., Lee, Y.J., Zhang, Y., Sorkin, A., Manzhos, S., Wang, H., 2022b. Effect of a weak magnetic field on ductile–brittle transition in micro-cutting of single-crystal calcium fluoride. J. Mater. Sci. Technol. 112, 96–113.

Guo, Y., Zhan, J., Lee, Y.J., Lu, W.F., Wang, H., 2023. Predictive modelling for enhanced scratching of brittle ceramics with magneto-plasticity. Int. J. Mech. Sci. 249, 108272.

Harvey, J.E., Schröder, S., Choi, N., Duparré, A., 2012. Total integrated scatter from surfaces with arbitrary roughness, correlation widths, and incident angles. Optical Engineering 51 (1), 013402.

Huang, W., Yan, J., 2023. Effect of tool geometry on ultraprecision machining of soft-brittle materials: a comprehensive review. Int. J. Extrem. Manuf. 5, 12003.

Kakinuma, Y., Azami, S., Tanabe, T., 2015. Evaluation of subsurface damage caused by ultra-precision turning in fabrication of CaF2 optical micro resonator. CIRP Ann. 64, 117–120.

Komiya, R., Kimura, T., Nomura, T., Kubo, M., Yan, J., 2018. Ultraprecision cutting of single-crystal calcium fluoride for fabricating micro flow cells. J. Adv. Mech. Des., Syst., Manuf. 12, M21.

Lee, Y.J., Chong, J.Y., Chaudhari, A., Wang, H., 2019. Enhancing ductile-mode cutting of calcium fluoride single crystals with solidified coating. Int. J. Precis. Eng. Manuf. -Green. Technol.

Lee, Y.J., Senthil Kumar, A., Wang, H., 2021. Beneficial stress of a coating on ductile-mode cutting of single-crystal brittle material. Int. J. Mach. Tools Manuf. 168, 103787.

Leung, T.P., Lee, W.B., Lu, X.M., 1998. Diamond turning of silicon substrates in ductile-regime. J. Mater. Process. Technol. 73, 42–48.

Li, Z., Fang, F., Chen, J., Zhang, X., 2017. Machining approach of freeform optics on infrared materials via ultra-precision turning. Opt. Express 25, 2051–2062.

Mizumoto, Y., Kakinuma, Y., 2018. Revisit of the anisotropic deformation behavior of single-crystal CaF2 in orthogonal cutting. Precis. Eng. 53, 9–16.

Mizumoto, Y., Aoyama, T., Kakinuma, Y., 2011. Basic study on ultraprecision machining of single-crystal calcium fluoride. Procedia Eng. 19, 264–269.

Mizumoto, Y., Kangawa, H., Itobe, H., Tanabe, T., Kakinuma, Y., 2017. Influence of crystal anisotropy on subsurface damage in ultra-precision cylindrical turning of CaF2. Precis. Eng. 49, 104–114.

Mukaida, M., Yan, J., 2017a. Ductile machining of single-crystal silicon for microlens arrays by ultraprecision diamond turning using a slow tool servo. Int. J. Mach. Tools Manuf. 115, 2–14.

Mukaida, M., Yan, J., 2017b. Fabrication of hexagonal microlens arrays on single-crystal silicon using the tool-servo driven segment turning method. Micromachines 8, 323.

Namba, Y., Ohnishi, N., Yoshida, S., Harada, K., Yoshida, K., Matsuo, T., 2004. Ultra-precision float polishing of calcium fluoride single crystals for deep ultra violet applications. CIRP Ann. 53, 459–462.

Namba, Y., Yoshida, T., Yoshida, S., Yoshida, K., Iwata, K., 2005. Surfaces of calcium fluoride single crystals ground with an ultra-precision surface grinder. CIRP Ann. 54, 503–506.

Sun, Z., To, S., Zhang, S., 2018. A novel ductile machining model of single-crystal silicon for freeform surfaces with large azimuthal height variation by ultra-precision fly cutting. Int. J. Mach. Tools Manuf. 135, 1–11.

Wang, H., Senthil Kumar, A., Riemer, O., 2016a. On the theoretical foundation for the microcutting of calcium fluoride single crystals at elevated temperatures. Proc. Inst. Mech. Eng., Part B: J. Eng. Manuf. 232, 1123–1129.

Wang, H., Riemer, O., Rickens, K., Brinksmeier, E., 2016b. On the mechanism of asymmetric ductile–brittle transition in microcutting of (111) CaF2 single crystals. Scr. Mater. 114, 21–26.

Wang, J., Wang, Y., Zhang, J., Yang, Y., Guo, P., 2021. Structural coloration of non-metallic surfaces using ductile-regime vibration-assisted ultraprecision texturing. Light.: Adv. Manuf. 2, 33.

Yan, J., Syoji, K., Tamaki, J.I., 2003. Crystallographic effects in micro/nanomachining of single-crystal calcium fluoride. J. Vac. Sci. Technol. B: Microelectron. Nanometer Struct. Process., Meas., Phenom. 22, 46–51.

Yan, J., Asami, T., Harada, H., Kuriyagawa, T., 2009. Fundamental investigation of subsurface damage in single crystalline silicon caused by diamond machining. Precis. Eng. 33, 378–386.

Yang, B., Zhou, J., Chen, Q., Lei, L., Wen, K., 2018. Fabrication of hexagonal compound eye microlens array using DMD-based lithography with dose modulation. Opt. Express 26, 28927–28937.

Yoshino, M., Aoki, T., Shirakashi, T., Komanduri, R., 2001. Some experiments on the scratching of silicon: In situ scratching inside an SEM and scratching under high external hydrostatic pressures. Int. J. Mech. Sci. 43, 335–347.

Yu, D.P., Wong, Y.S., Hong, G.S., 2011. A novel method for determination of the subsurface damage depth in diamond turning of brittle materials. Int. J. Mach. Tools Manuf. 51, 918–927.

Yu, D.P., Gan, S.W., Wong, Y.S., Hong, G.S., Rahman, M., Yao, J., 2012. Optimized tool path generation for fast tool servo diamond turning of micro-structured surfaces. Int. J. Adv. Manuf. Technol. 63, 1137–1152.

Yuan, Y., Zhang, D., Jing, X., Ehmann, K.F., 2020. Freeform surface fabrication on hardened steel by double frequency vibration cutting. J. Mater. Process. Technol. 275, 116369.

Zhang, J., Zhang, J., Liu, C., Chen, X., Xiao, J., Xu, J., 2020b. Machinability of single crystal calcium fluoride by applying elliptical vibration diamond cutting. Precis. Eng. 66, 306–314.

Zhang, L., Zhou, W., Naples, N.J., Yi, A.Y., 2018. Fabrication of an infrared Shack-Hartmann sensor by combining high-speed single-point diamond milling and precision compression molding processes. Appl. Opt. 57, 3598–3605.

Zhang, L., Naples, N.J., Zhou, W., Yi, A.Y., 2019. Fabrication of infrared hexagonal microlens array by novel diamond turning method and precision glass molding. J. Micromech. Microeng. 29, 65004.

Zhang, L., Zhou, L., Zhou, W., Zhang, S., Yi, A.Y., 2020a. Design, fabrication and testing of a compact large-field-of-view infrared compound eye imaging system by precision glass molding. Precis. Eng. 66, 87–98.

Zhang, L., Zolfaghari, A., Zhou, W., Shu, Y., Yi, A.Y., 2022. Flexible metallic mold based precision compression molding for replication of micro-optical components onto non-planar surfaces. Precis. Eng. 76, 149–159.

Zhou, T., Zeng, Z., Yu, Q., Zhou, J., Liu, P., Wang, X., 2023. Study on gas trapping during precision glass molding of microlens array in a nitrogen atmosphere. *Int. J. Appl. Glass Sci., N./a.*

Zhu, W., Duan, F., Zhang, X., Zhu, Z., Ju, B., 2018. A new diamond machining approach for extendable fabrication of micro-freeform lens array. Int. J. Mach. Tools Manuf. 124, 134–148.